

Artificial Intelligence-based Motion Tracking in Cancer Radiotherapy: A Review

Elahheh Salari¹, Jing Wang¹, Jacob Wynne², Chih-Wei Chang¹ and Xiaofeng Yang^{1*}

¹Department of Radiation Oncology, Emory University School of Medicine, Atlanta, GA 30322

²Department of Radiation Oncology, Icahn School of Medicine at Mount Sinai, New York, NY 10029

***Corresponding author:**

Xiaofeng Yang, PhD

Department of Radiation Oncology

Emory University School of Medicine

1365 Clifton Road NE

Atlanta, GA 30322

E-mail: xiaofeng.yang@emory.edu

Abstract

Radiotherapy aims to deliver a prescribed dose to the tumor while sparing neighboring organs at risk (OARs). Increasingly complex treatment techniques such as volumetric modulated arc therapy (VMAT), stereotactic radiosurgery (SRS), stereotactic body radiotherapy (SBRT), and proton therapy have been developed to deliver doses more precisely to the target. While such technologies have improved dose delivery, the implementation of intra-fraction motion management to verify tumor position at the time of treatment has become increasingly relevant. Recently, artificial intelligence (AI) has demonstrated great potential for real-time tracking of tumors during treatment. However, AI-based motion management faces several challenges including bias in training data, poor transparency, difficult data collection, complex workflows and quality assurance, and limited sample sizes. This review serves to present the AI algorithms used for chest, abdomen, and pelvic tumor motion management/tracking for radiotherapy and provide a literature summary on the topic. We will also discuss the limitations of these algorithms and propose potential improvements.

Keywords: Artificial intelligence, Radiotherapy, Motion Tracking, Intrafraction motion

1. Introduction

Radiotherapy aims to deliver a high dose of radiation to treatment targets while minimizing the dose to surrounding healthy tissues. The advent of flattening filter-free (FFF) treatment delivery brought higher dose rate beams and greater normal tissue sparing due to the sharp dose fall-off outside the tumor (1, 2). The FFF technique has widened the therapeutic window, ushering in new radiation delivery techniques such as SRS and SBRT (2, 3). Intrafraction motion monitoring is particularly needed for the SRS and SBRT, where a high dose is delivered to the target in a few fractions, and narrow margins are needed to spare healthy tissues (4). This treatment technique is commonly implemented in the lung, abdomen, and sometimes pelvis, where the efficiency of the treatment can be significantly reduced due to intrafraction respiratory, cardiac, gastrointestinal, and urinary motion during the treatment (5-7). Internal organ movement may cause underdosing or overdosing of targets or normal tissues, potentially causing treatment failure and increasing normal tissue toxicity (8-10). In this setting, real-time tumor tracking techniques are essential to localize targets and ensure accurate treatment delivery without compromising treatment quality due to motion. Conventional motion management techniques include: using a dynamic multileaf collimator (MLC) to optimize MLC positions based on target motion (11), adjusting the radiation beam and robotic couch according to target movement (12), implanting electromagnetic transponders in the soft tissue to localize tumors or placing transponders on the body surface to monitor the motion (13, 14), utilizing stereoscopic kilovoltage (kV) imaging in conjunction with a six-degrees-of-freedom couch (15), employing an optical surface tracking system using an infrared camera to automatically align patients by tracking infrared (IR) markers on their skin or a rigid template (16), and using ultrasound (US) guidance equipped with a hardware device to hold a US probe in a position that maintains the target within the US imaging field of view during the treatment session (17). Recently, magnetic resonance imaging (MRI) integrated with the linear accelerator has been developed for monitoring intrafractional motion during dose delivery (18). The purpose of this review is not to provide a detailed explanation of each technique, interested readers are directed to Wu et al (19), which contains additional information.

Though various methods for intrafraction motion management have been developed (19), direct detection of the target during the treatment is often not feasible (20). Alternatively, indirect tumor localization facilitated with artificial intelligence (AI) approaches can be used. After decades of development, modern AI approaches can be categorized into machine learning (ML) and deep learning (DL). When applied to motion management, these techniques have achieved great success in analyzing medical images and making motion predictions. AI-based techniques can be applied to several disease sites as well as many imaging modalities including MRI, computed tomography (CT), and US. Due to the wide range of possible applications, numerous motion-tracking strategies have been proposed. Recently, ML approaches

integrating radiomics have been developed to analyze medical images. Radiomics is a novel topic in the field of radiology, which extracts mineable quantitative features from medical images. The extracted features contain information on size, shape, and texture from the region of interest and can be used to develop ML models to predict target position (20, 21). Traditional algorithms including artificial neural network (ANN) (22), support vector machine (SVM) (23), light gradient boosting machine (LightGBM) (21), decision trees (DT) (20), random forests (RF) (24) have also been used for predicting tumor position.

In addition to classic ML approaches, many authors have employed DL for real-time tracking of tumors. Convolutional neural network (CNN) is one of the backbone DL architectures used in various medical image/object recognition and classification (25-27). A typical CNN has an initial input layer, and a final output layer with several intervening “hidden” layers connecting the input and output. In CNNs, the hidden layers extract higher-level image “features” from the input image, typically across several resolutions, capturing detail at several spatial scales. A hidden layer may include convolution, pooling, and rectified linear units, in addition to many others. Other more advanced networks such as recurrent neural network (RNN) (28), region convolutional neural network (R-CNN) (29), Siamese networks (30), you-only-look-once (YOLO) (31), long short-term memory (LSTM) (32), and encoder-decoder networks (33) have been introduced for real-time tumor tracking. A detailed taxonomy of DL network architectures is out of the scope of the present article but can be found in a recent review by Wang *et al* (34).

This work aims to review AI-based approaches for tumor tracking in the thoracic, abdominal, and pelvic regions, discuss present limitations, and provide potential solutions for more accurate outcomes.

2. Literature Search

This review focuses on intrafraction motion management using classic ML and DL algorithms. To ensure this systematic review is valuable to users, we followed the Preferred Reporting Items for systematic reviews and meta-analyses (PRISMA) (35). For this aim, we only considered peer-reviewed papers as they undergo an evaluation process where journal editors and experts critically assess the article's quality and scientific merit. In this regard, the PubMed search engine was used with a time window from January 2005 to August 2023. The search keywords were limited to “cancer or radiotherapy”, “deep learning or machine learning or artificial intelligence”, “imaging or image-guided radiation therapy or IGRT”, and “motion”. The initial search yielded 173 records. However, after excluding literature reviews and publications not related to medicine, only 87 papers remained. Moreover, a citation search was conducted on other literature resulting in an additional 17 papers; therefore, a total of 104 articles were included in this review study. Figure 1 shows the surging number of yearly peer-reviewed publications containing the terms “artificial intelligence/machine learning/deep learning”, “motion”, “radiotherapy/cancer”, and “images” from 2010 to August 2023 in the PubMed database (www.pubmed.gov). Figures 2 and 3 display the percentage of

studies for each treatment site and imaging modality, respectively. X-ray includes CT, cone beam CT (CBCT), four-dimensional CT (4DCT), and kV fluoroscopic images. Other modalities include MV and optical surface monitoring.

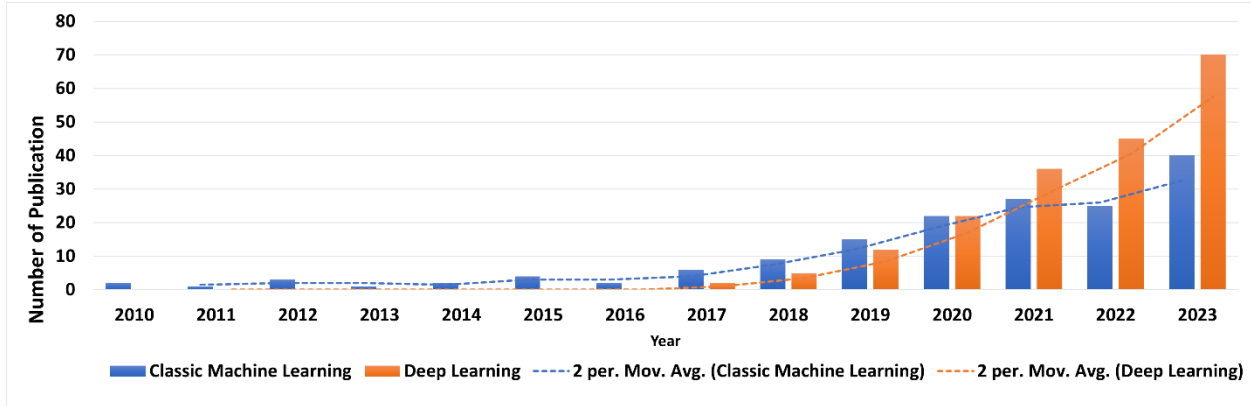


Figure 1. Number of publications using classic ML & and DL-based motion management since 2010. Deep learning has exponentially increased since 2017. The number of publications in 2023 is an estimation based on the number of publications from January to August 2023.

TREATMENT SITES

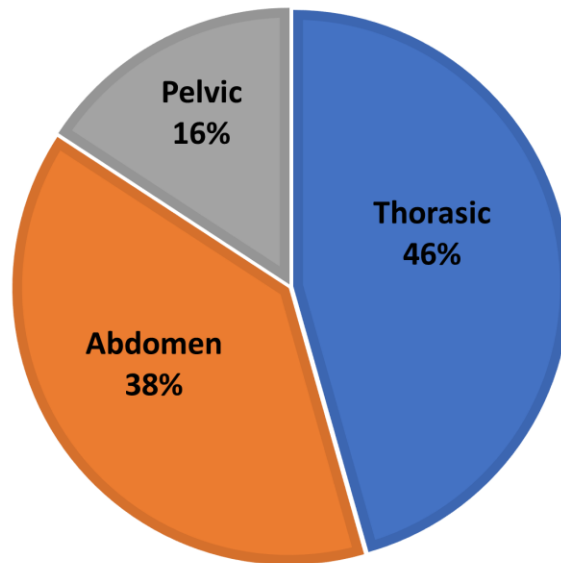


Figure 2. The percentage of studies conducted on each treatment site using AI-based motion management in PubMed (www.pubmed.gov) since 2005.

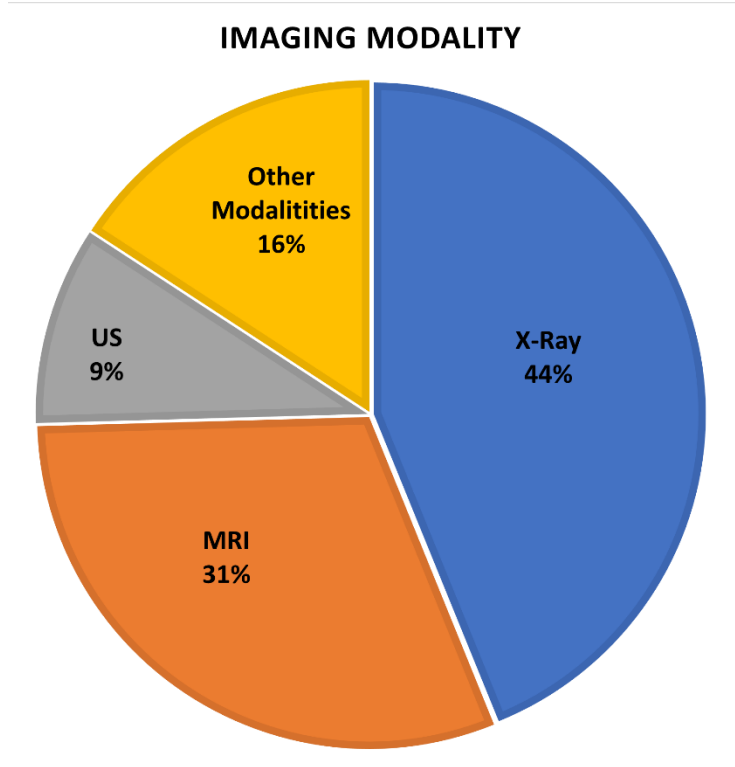


Figure 3. The percentage of each modality in AI-based motion tracking in PubMed (www.pubmed.gov) since 2005. X-ray includes CT, CBCT, 4DCT, MV, and kV fluoroscopic images. Other modalities include respiratory gating, electromagnetic transponders, and optical surface monitoring.

3. Motion management for various treatment sites

3.1. Thoracis

According to the American Cancer Society, lung cancer is the leading cause of cancer-related death in the United States (36). Thus, lung cancer has been extensively studied. Radiotherapy is a standard of care in the multi-disciplinary treatment of lung cancer and is being increasingly used but is challenged by intrafraction motion during treatment. Intrafraction motion is primarily a result of respiration, with a lesser contribution of the cardiac cycle to tissue displacement and deformation. Respiration induces organ motion and anatomical shifts which can significantly reduce the accuracy of dose delivery, causing failure of tumor control or normal tissue injury (37). Respiratory gating and breath-hold are common solutions to manage target motion (38), but both techniques provide only a limited representation of the complex respiratory motion pattern (39). To solve this problem, several AI methods across several imaging modalities have been developed. A summary of these approaches in Table 1 demonstrates the majority of authors used X-rays (e.g., CT, CBCT, 4DCT, kV X-ray) in the chest area. In a standard CBCT scan of the thoracic region, respiration results in motion artifact. To minimize artifacts, inspiratory breath-hold was once commonly employed during CBCT image acquisition (40); however, modern chest radiotherapy now uses respiratory

time-series imaging (4DCT) to capture physiologic motion throughout the breathing cycle (38). When it comes to examining tissue abnormalities in the chest, CT scans are more effective than MRIs. This is because MRI is a functional imaging technique based on water diffusivity. CT scans, on the other hand, can precisely detect lesions in the thoracic regions due to sharp differences in tissue density (41).

Table 1. Summary of publication using artificial intelligence for thoracic tumor tracking

Author	Year	AI model	Image modality	No. samples	Key findings in results
Isaksson et al (42)	2005	Linear filters, adaptive linear filters, and adaptive neural networks (Feed-forward neural networks)	kV X-ray	3 (1 pancreatic, 2 lung cancer patients)	The neural network (NN) achieved better tracking accuracy than other algorithms. The NN was able to predict the position of the tumor up to 800 ms in advance. In one case, the linear filter was completely unable to predict the tumor position ($nRSME = 100\%$).
Kakar et al (43)	2005	Adaptive neuro-fuzzy inference system (ANFIS)	Infrared camera	11 lung cancer patients	Root-mean-square error (RMSE) for coached patients was 6% and for non-coached patients (breath freely) was 35% over an interval of 20 seconds.
Murphy and Dieterich (44)	2006	The linear adaptive filter and the adaptive nonlinear neural network	Optical tracking system	9 lung cancer patients	Predict respiratory signals up to 1 second in advance. The neural network outperformed the linear filter. In some cases, the linear filter was completely unable to adapt to the breathing signal
Yan et al (45)	2006	ANN	The signal of a simulator and IR camera	4 patients	The target position can be predicted using external surrogates if the correlation between internal target motion and external marker signals is consistent.
Zhang et al (46)	2007	Principal component analysis (PCA)	CT	4 lung cancer patients	The average discrepancies between the predicted model and ground truth were 1.1 ± 0.6 mm LR, 1.8 ± 1.0 mm AP, and 1.6 ± 1.4 mm SI.
Cui et al (23)	2008	SVM	kV X-ray	5 lung cancer patients	The SVM can predict the gating signal to deliver the dose to the target with tumor coverage greater than 90%.
Lin et al (47)	2009	ANN, SVM	kV X-ray	9 lung cancer patients (ten fluoroscopic image sequences)	ANN approach is more accurate than SVM in terms of classification accuracy and recall rate. The ANN achieved higher accuracy than SVM (96.3 ± 1.6 vs 94.9 ± 1.7). The average running time for ANN is less than SVM (6.7 ms vs. 11 ms).
Lin et al (48)	2009	Linear regression (LR), two-degree polynomial regression, ANN, and SVM	kV X-ray	10 lung cancer patients	Two-degree polynomial regression tends to be overfitted. ANN performs better and is more robust than the other models. ANN achieved the lowest localization errors within all models.
Riaz et al (49)	2009	Multidimensional adaptive filter, SVM	Optical tracking system	14 lung cancer patients	The SVM prediction results are more accurate than the other model with the RSME equal to 1.26. The RMSE of the multidimensional adaptive filter was 1.71.
Torshabi et al (50)	2010	ANN and Fuzzy logic	Cyberknife® Synchrony	15 chest cases and 4 abdominal cases (10 worse cases, 10 control cases)	The best performance was obtained using Fuzzy logic algorithms. The result of ANN was comparable to Cyberknife Synchrony and the calculation time of ANN was higher than other models. The error reduction with respect to Synchrony®, measured at the 95% confidence level is 10.8% for the fuzzy logic approach and 8.7% for ANN.
Cervino et al (51)	2011	ANN, template matching algorithm with surrogate tracking using the diaphragm	MRI	5 healthy volunteers	The matching approach detects the target position more accurately than the ANN model.
Krauss et al (52)	2011	LR, NN, kernel density estimation, and SVM	kV X-ray	12 breathing data	When considering all sampling rates and latencies, the observed prediction errors normalized to errors of using no prediction for NN, SVR, LR, and KDE were 0.44, 0.46, 0.49, and 0.55 respectively.

Li et al (53)	2011	PCA	4DCT	Two phantoms and 11 image sets from eight patients.	The modeling error was within 0.7 ± 0.1 mm. The mean 3D error was 1.8 ± 0.3 mm.
Fayad et al (54)	2012	PCA	4DCT and synchronized RPM signal	10 lung cancer patients	The model is substantially accurate when it includes both phase and amplitude data with the model error of 1.35 ± 0.21 mm.
Yun et al (22)	2012	ANN (feed-forward neural network)	MRI (MR-linac)	29 lung cancer patients	For 120–520 ms system delays, mean RMSE values of 0.5–0.9 mm (ranges 0.0–2.8 mm from 29 patients) were observed.
Torshabi et al	2014	ANFIS	Cyberknife@Synchrony	10 (lung and pancreas cancer patients)	The ANFIS model was able to decrease tumor tracking errors significantly compared with the ground truth database and even their previous study (50).
Li et al (55)	2015	MLR	4DCT	11 lung cancer patients (2 scans for each patient so 22 4DCT in total)	The ML model was able to predict the diaphragm motion with acceptable error (0.2 ± 1.6 mm).
W Bukhari and S-M Hong (56)	2015	An extended Kalman filter (LCM-EKF) to predict the respiratory motion and a model-free Gaussian process regression (GPR) to correct the error of the LCM-EKF prediction.	Gating system	31 patients (304 traces of respiratory motion)	This model reduced the root-mean-square error by 37%, 39%, and 42% for a duty cycle of 80% at lookahead lengths of 192 ms, 384 ms, and 576 ms respectively compared to the non-correction method.
Yun et al (57)	2015	ANN	MRI (MR-linac)	One phantom and four lung cancer patients	The phantom study yields a mean Dice similarity index (DSI) of 0.95–0.96, and a mean Hausdorff distance (HD) of 2.61–2.82 mm. The mean DSI of 0.87–0.92, with a mean HD of 3.12–4.35 mm for the patient study.
Bukovsky et al (58)	2015	Multilayer perceptron (MLP), Quadratic Neural Unit (QNU)	3D time series of lung motion	356 simulations for QNU and 2475 for MLP	The mean absolute error was 0.987 mm and 1.034–1.041 mm for QNU and MLP respectively. The QNU model provided better results with a mean absolute error of 0.987 and was faster than MLP.
Park et al (59)	2016	Fuzzy deep learning (FDL), CNN, Hybrid motion estimation based on extended Kalman filter (HEKF)	CyberKnife Synchrony	130 lung cancer patients	FDL showed fewer variations than CNN and HEKF. The RMSE of FDL was 30 % better than CNN and HEKF. The average computing time using a central processing unit (CPU) for FDL, CNN, and HEKF was 1.54 ± 5.01 ms, 254.32 ± 11.68 ms, and 253.56 ± 10.74 ms respectively.
Teo et al (60)	2018	A 3-layer perceptron neural network	MV images	47 (27 in group 1 and 20 in group 2, unseen data)	The average MAE (group 1) = 0.59 ± 0.13 mm, and the average MAE (group 2) = 0.56 ± 0.18 mm. The average RMSE (group 1) = 0.76 ± 0.34 mm and for group 2 was 0.63 ± 0.36 mm.
Terunuma et al (61)	2018	CNN	3D CT	For training and testing data sets, 2000 and 300 pairs of model and supervised images were used respectively	The proposed method achieved accurate tumor tracking of low visibility tumors of over 0.95 based on the Jaccard index, and accurate tumor tracking with an error of approximately 1 mm.
Edmunds et al (62)	2019	Region-CNN (R-CCN)	CBCT	10 lung cancer patients (3500 raw CBCT projection images)	The performance of the model was lower at lateral angles when larger amounts of fatty tissue obstructed the view of the diaphragm. The model could estimate the diaphragm apex positions with a mean error of 4.4 mm.
Jiang et al (63)	2019	A non-linear autoregressive model with exogenous input (NARX)	Gating system	7 lung cancer patients	Mean \pm standard deviation was $82.32\pm 17.93\%$, $80.52\pm 18.00\%$, and $79.77\pm 18.42\%$ of three different prediction horizons, 600 ms, 800 ms, and 1 s respectively.
Lin et al (24)	2019	A model was a combination of four base machine learning algorithms such as the RF, MLP, LightGBM, and XGBoost.	4DCT and the Electronic Health Record	150 lung cancer patients	The maximum MAE and RMSE were in the superior-inferior (SI) direction with 1.23 mm and 1.70 mm respectively.
Hirai et al (64)	2019	DNN	4DCT	5 lung cancer patients and 5 liver cancer patients. Each 4DCT	Averaged track accuracy was 1.64 ± 0.73 mm. Accuracy for liver cases was 1.37 ± 0.81 mm and for lung cases was 1.9 ± 0.65 mm. Computation time was less than 40 ms

				contains 10 respiratory phases	
Lei et al (7)	2020	The transNet model consists of three modules (encoding, transformation, and decoding modules)	3D CT generated from 2D CT	20 lung cancer patients	The mean value of the center of mass distance between manual tumor contours on the ground images and corresponding 3D CT images derived from 2D projection was 1.26 mm, with a maximum deviation of 2.6 mm. The peak signal-to-noise ratio was 15.4 ± 2.5 decibel (dB) and the structural similarity index metric within the tumor region of interest was 0.839 ± 0.090 .
Mori et al (65)	2020	DNN	4DCT derived from 3DCT	Train set: 2420 thoracic 4DCT from 436 patients Test set: 20 lung cancer patients	The averaged tracking positional errors were 0.56 mm, 0.65 mm, and 0.96 mm in the X, Y, and Z directions, respectively.
Sakata et al (66)	2020	Extremely randomized trees (ERT)	4DCT	8 lung cancer patients	The average tracking positional accuracy was 1.03 ± 0.34 mm (mean \pm standard deviation, Euclidean distance) and 1.76 ± 0.71 mm (95th percentile).
Dai et al (67)	2021	Markov-like network	US	The Cardiac Acquisitions for Multi-structure Ultrasound Segmentation (CAMUS) dataset includes 2D US images from 450 patients. The Challenge on Liver Ultrasound Tracking (CLUST) dataset consists of 63 2D and 22 3D image sequences from 42 patients and 18 patients	CLUST dataset: A mean tracking error of 0.70 ± 0.38 mm for the 2D point landmark tracking and 1.71 ± 0.84 mm for the 3D point landmark tracking. CAMUS dataset: A mean TE of 0.54 ± 1.24 mm for the landmarks in the left atrium
He et al (68)	2021	ResNet generative adversarial network	kV X-ray	20 Patients (1347 2D kV images thoracic and lumbar regions)	The mean error with the decomposed image and the original DRR was 0.13, 0.12, and a maximum of 0.58, and 0.49 in the x- and y-directions (in the imager coordinates), respectively.
Momin et al (29)	2021	R-CCN, VoxelMorph, U-Net, networks without global and local networks, and networks without attention gate strategy	4DCT	First experiment (Training set: 20 4DCT, Test set: additional 20 4DCT) The second experiment (training set: 40 4DCT, test set: 9 additional unseen 4DCT). Each 4DCT contains 10 breathing phases	The method was evaluated against several other networks, including VoxelMorph, U-Net, and networks without global or local networks or attention-gate strategies. The Dice similarity coefficients of experiments 1 and 2 were higher than those achieved by VoxelMorph, U-Net, network without global and local networks, and networks without attention gate strategy. Specifically, experiment 1 achieved a coefficient of 0.86 compared to 0.82, 0.75, 0.81, and 0.81 achieved by the aforementioned methods, and experiment 2 achieved a coefficient of 0.90 compared to 0.87, 0.83, 0.89, and 0.89 achieved by the aforementioned methods.
Pohl et al (28)	2021	RNN, linear predictor (LP), least mean squares (LMS)	4D CBCT and 4DCT	4 lung cancer patients (Chest 3D 16-bit image sequences). Each sequence had 10 3D images of the chest at different phases of breathing	RNN was superior to LP and LMS. The maximum prediction error for RNN, LP, and LMS was 1.51 mm, 1.80 mm, and 1.59 mm respectively. RMSE was 0.444 mm, 0.449 mm, and 0.490 mm for RNN, LP, and LMS respectively. The Jitter of RNN, LP, and LMS was 2.59 mm, 2.59 mm, and 2.63 mm respectively.
Terpstra et al (26)	2021	A multiresolution CNN called TEMPEST	MRI	27 lung cancer patients (training set:17, validation set:5, test set: 5). Also, the model was evaluated using the publicly available 4DCT dataset.	Compared to the self-navigation signal using 50 spokes per dynamic (366 \times undersampling), the model was able to provide more accurate motion estimation results. Deformation vector fields were estimated to be within 200 ms, including MRI acquisition. The target registration error of the model on 4DCT without retraining was 1.87 ± 1.65 mm.

Liu et al (69)	2022	NuTracker model using MLP	4DCT	7 lung cancer patients with gold fiducial markers	The proposed model had 26% and 32% improvement over the predominant linear methods with the mean localization error of 0.66 mm and <1 mm at the 95 th percentile.
Lombard et al (70)	2022	LSTM, LR	MRI	Training and validation set: 70 patients from group 1. The test set includes 18 patients from Group 1 and 3 patients from Group 2	LSTM outperformed compared to the LR model. For the 500 ms forecasted interval, a mean RMSE of 1.20 mm and 1.00 mm were obtained for LSTM, while the LR model yielded a mean RMSE of 1.42 mm and 1.22 mm for the group 1 and group 2 testing sets, respectively.
Zhang et al (21)	2022	Light gradient boosting machine-based recursive feature elimination with radiomics features	4DCT	67 lung cancer patients	Mean \pm standard deviation was 0.8 ± 0.126 , 0.829 ± 0.14 , and 0.864 ± 0.086 for thresholds of 0.7, 0.8, and 0.9 respectively. The specificities were 0.771 ± 0.114 , 0.936 ± 0.0581 , and 0.839 ± 0.101 . The area under the curve (AUC) was 0.837, 0.946, and 0.877, respectively.
Hindley et al (71)	2023	Voxelmap network	CBCT	2 lung cancer patients (6120 images for training, 680 images for validation, and 680 images for testing).	The mean errors of 3D tumor motion prediction were 0.1 ± 0.5 , -0.6 ± 0.8 , and 0.0 ± 0.2 mm in the left-right, SI, and anterior-posterior directions respectively.
Huttinga et al (72)	2023	Gaussian process	MRI (MR-linac)	One phantom, one healthy volunteer, one patient	The root-mean-square distances and mean end-point-distance with the reference tracking method were less than 0.8 mm for all cases.
Lombard et al (73)	2023	Classical LSTM network (LSTM-shift), Convolutional LSTM (convLSTM), and convLSTM with spatial transformer layers (convLSTM-STL)	MRI	88 patients (training:52, validation: 18, and test:21)	The LSTM-shift model was found to be significantly better than other models. The maximum RMSE of LSTM-shift was 1.3 ± 0.6 mm. convLSTM and convLSTM-STL yielded the maximum RMSE of 1.9 ± 1.1 and 1.9 ± 1.0 mm respectively.
Zhou et al (74)	2023	DNN	kV X-ray	10 lung cancer patients (2250 digitally reconstructed radiographs)	The mean calculation time was 85 ms per image. The median value for the 3D deviation was 2.27 mm overall. There is a 93.6% chance that the 3D deviation is less than 5 mm.
Li et al (20)	2023	multilayer perceptron (MLP), wide and deep (W&D), categorical boosting (Cat), light gradient boosting machine (Light), extreme gradient boosting (XGB), adaptive boosting (Ada), random forest (RF), decision tree (DT), logistic regression via stochastic gradient descent (SGD), gaussian naive bayes (GNB), support vector classifiers (SVC), linear support vector classifiers (linearSVC), and K-nearest neighbor (KNN)	CT	108 lung cancer patients	The best result in terms of AUC was obtained by SVC (0.941). Linear SVC provided the best outcome in terms of sensitivity (0.848). The best specificity results were achieved using MLP (0.936). In general, MLP demonstrated the best classification performance and stability among all models.

3.2. Abdomen

Radiation therapy for gastrointestinal cancers often faces two main physical challenges. The first is the proximity of the tumor(s) to many essential OARs such as the duodenum, stomach, small intestine, kidneys, or spinal cord at the level of the abdomen. The second is the mobility typical of both the target and nearby OARs (75). In the abdomen, respiration, peristalsis, and variable organ filling result in variation in target position and organ deformation. The advent of advanced treatment techniques such as volumetric

modulated arc therapy (VMAT) and SBRT solved the first challenge by providing highly conformal 3D dose distributions. However, the effective delivery of such a conformal dose to the target requires careful motion management (31, 75). In addition to gating respiratory and breath hold, using an abdominal compression plate is a primary strategy for motion management in the abdomen. AI may be used to augment motion-tracking techniques due to its capability to assess several aspects simultaneously. The summary of these AI-based approaches can be found in Table 2. which indicates MRI is of particular interest because abdominal regions are composed primarily of soft tissue. US can also be used for monitoring anatomical movements in soft tissue and is particularly effective in monitoring hepatic and pancreatic targets due to site accessibility and the absence of osseous obstruction (18).

Table 2. Summary of publication using artificial intelligence for abdomen tumor tracking

Author	Year	Algorithm	Image Modality	No. Patients	Key findings in results
Gou et al (76)	2016	Dictionary learning model	MRI	3 pancreatic patients and two healthy volunteers (total of 12 imaging volumes)	The dictionary method improved the auto-segmentation, at least 1 of the auto-segmentation method with Dice's index > 0.83 and shift of the center of the organ was less than equal to 2 mm.
Stemkens et al (77)	2016	PCA	MRI	Phantom and 7 healthy volunteers (Pancreas and kidney)	An average error of 1.45 mm with a temporal resolution < 500 ms was achieved.
Ozkan et al (78)	2017	Supporters (proposed by Grabner et al (79)) with Leave-one-out cross-validation	US	24 2D image sequences of Liver	The results for all targets were a mean of 1.04 mm and 2.26 mm 95% percentile tracking error.
Dick et al (80)	2018	ANN	4DCT	4D extended cardiac-torso (XCAT) phantom	The RMSE for the lung-defined tumor motion was 0.67 mm and for the user-defined tumor motion was 0.32 mm. The RMSE of ANN for mismatched data was 1.63 mm, and for the ground-truth data, the RMSE was obtained at 0.88 mm.
Dick et al (81)	2018	ANN with Leave-one-out-cross-validation	4DCT	4D extended cardiac-torso (XCAT) phantom and 8 liver patients	The averaged RMSE was 1.05 ± 1.14 mm and 2.26 ± 2.4 mm for phantom and patients' data respectively.
Huang et al (82)	2019	k-dimensional-tree-based nearest neighbor search	US	57 different anatomical features were acquired from 27 sets of 2D ultrasound sequences.	The mean tracking error between manually annotated landmarks and the location extracted from the indexed training frame is 1.80 ± 1.42 mm. Adding a fast template matching can reduce the mean tracking error to 1.14 ± 1.16 mm.
Huang et al (83)	2019	FCN with convolutional LSTM (CLSTM)	US	The train set was 25 and the test set was 39 liver cancer patients	The mean and maximum tracking error were 0.97 ± 0.52 mm and 1.94 mm respectively. The tracking speed using GPU was from 66 to 101 frames per second.
Zhao et al (84)	2019	A patient-specific region-based convolutional neural network (PRCNN)	kV X-ray	2 pancreatic cancer patients (2400 DRR datasets)	The mean absolute difference between the model-predicted and the actual positions < 2.60 mm in all directions. Lin's concordance correlation coefficients between the predicted and actual positions were > 93%.
Liang et al (85)	2020	FCN	Cyberknife® Synchrony	13 liver cancer patients (5927 images)	The mean centroid error between the predicted and the ground truth was 0.25 ± 0.47 pixels on the test dataset. The maximum mean translation was seen in the SI direction with 13.1 ± 2.2 mm.

Liu et al (86)	2020	SVM	Cyberknife® Synchrony	148 liver cases and 48 cases of other anatomical sites (e.g., Kidney, pancreas)	The sensitivity, precision, specificity, F1 score, and accuracy are 0.81 ± 0.09 , 0.85 ± 0.08 , 0.80 ± 0.11 , 0.83 ± 0.06 , and 0.80 ± 0.07 , respectively. An AUC of 0.87 ± 0.05 was achieved.
Roggen et al (87)	2020	Mask R-CNN	CBCT	Train set: 12 abdominal cancer patients (903 images). Test set: 1 patient (49 images) and one phantom with vertebrae	This paper presents a fast DL model for detecting landmarks in vertebrae and evaluates its accuracy in detecting 2D motion using projection images taken during treatment. The proposed network was able to detect the motion in both translational and rotational variations, with sub-millimeter accuracy.
Terpstra et al (88)	2020	The convolutional neural network called SPyNET	MRI	7 abdomen, 40 liver, 62 kidney, and 26 pancreas cancer patients (200 images)	Combining non-uniform fast Fourier transform with SPyNET resulted in acceptable performance for 25-fold accelerated data, yielding an imaging frame rate of 25 Hz while keeping the RMSE within 1 mm.
Bharadwaj et al (30)	2021	Upgraded Siamese neural network using Linear Kalman filter (LKF)	US	CLUS	The proposed model enhanced the Siamese neural network by resolving the constant position model issue and improving robustness. In order to improve the original architecture, LKF was added to include the missing motion model.
Romaguera et al (89)	2021	Encoder-decoder network	MRI, US	MRI: 25 volunteers, and 11 patients diagnosed with hepatocellular carcinoma. US: 20 volunteers.	The model used image surrogates for volumetric prediction and yielded mean errors of 1.67 ± 1.68 mm and 2.17 ± 0.82 mm for unseen MRI and US patient datasets respectively.
Shao et al (90)	2021	U-Net	CBCT	34 liver cancer patients (train set:24, test set:10)	The model obtained the mean center of mass error of 4.7 ± 1.9 mm, 2.9 ± 1.0 mm, and 1.7 ± 0.4 mm, the average DICE coefficients of 0.60 ± 0.12 , 0.71 ± 0.07 , and 0.78 ± 0.03 , and the mean Hausdorff distances of 7.0 ± 2.6 mm, 5.4 ± 1.5 mm, and 4.5 ± 1.3 mm, for 2D-3D, 2D-3D deformable registration with biomechanical modeling, and DL model prediction with biomechanical modeling techniques respectively.
Wang et al (32)	2021	LSTM, SVM	4D US and template matching to track the motion	7 volunteers	LSTM was superior to SVM with RMSE less than 0.5 mm at a latency of 450 ms for the prediction of respiratory motion and internal liver motion of < 0.6 mm.
He et al (91)	2021	ResNet generative adversarial network (ResNetGAN)	CT	Train set: 20 patients (1347 2D kV thoracic and lumbar region). Test set: 4 patients (226 2D kV images)	The model was able to enhance image quality for submillimeter accuracy. The decomposed spine image was matched with the ground truth with an average error of 0.13, 0.12, and a maximum of 0.58, and 0.49 in the x- and y-directions respectively.
Liu et al (92)	2022	DNN	MRI	7 liver cancer patients	The proposed model increased the image quality in terms of structural similarity index, peak signal noise ratio, and mean square error. The median distance between the predicted model and the ground truth in the SI direction was 0.4 ± 0.3 mm and 0.5 ± 0.4 mm for cine and radial acquisitions respectively.
Shao et al (93)	2022	RegNet, KS-RegNet-nup, and KS-RegNet	MRI	Eight cases from an open-access multi-coil k-space dataset (OCMR) were used for the cardiac dataset, 9 liver cancer patients for the abdominal dataset were selected.	KS-RegNet was found to be better, and more stable performance compared to other models.

Shao et al (94)	2022	Graph neural network or GNN	4DCT	10 liver cancer patients and each patient had 10 respiratory phases	The mean localization error was less than 1.2 mm. This indicates the potential of the model for tumor tracking.
Ahmed et al (31)	2023	CNN, YOLO, and CNN-YOLO	kV X-ray	training data (44 fractions, 2017 frames). Test data (42 fractions, 2517 frames)	The MAE and RMSE of all 3 models were less than 0.88 ± 0.11 mm and 1.09 ± 0.12 mm respectively.
Dai et al (95)	2023	CNN	Optical surface monitoring, and kV X-ray	7 liver cancer patients	The maximum MAE and RMSE were observed in the SI direction (3.12 ± 0.80 mm, and 3.82 ± 0.98 mm respectively).
Hunt et al (96)	2023	DL (VoxelMorph and U-Net), Affine, b-Spline, and demons	MRI	21 patients with abdominal or thoracic tumors (>629000 frames from 86 treatment fractions)	The DL model provided better results compared to conventional methods. The RMSE was 0.067, 0.040, 0.036, and 0.032 for affine, b-spline, demons, and DL respectively.
Shao et al (97)	2023	DL-based framework (Surf-X-Bio)	kV X-ray and surface imaging	34 liver cancer patients	The Surf-X-Bio can precisely monitor liver tumors through a combination of surface and x-ray imaging compared to surface-image-only and x-ray only models.

3.3.Pelvis

According to the American Cancer Society, prostate cancer is the most common malignancy of men in the US, accounting for 27% of the total diagnoses of all sites (36). Thus, prostate cancer has been widely studied. Radiotherapy is indicated as a primary and salvage treatment for prostate cancer in both early and advanced diseases. The major challenge of prostate radiation therapy is unpredictable intrafraction prostate motion due to variable rectal and bladder filling. Target position uncertainties in prostate cancer radiotherapy are usually addressed by assigning a margin around the target volume (98-100). However, without continuous monitoring and intervention, intrafraction motion can cause a geographic miss in approximately 10% of SBRT prostate therapy cases (5). Various strategies have been proposed for intrafraction motion monitoring such as US, kV/kV imaging, infrared cameras, implanted fiducial markers with in-room imaging, CBCT, and MRI (99, 100). Among these, fiducial markers used in conjunction with X-ray imaging is most commonly employed, allowing for real-time target localization and tracking (101, 102). However, even with appropriate use, marker migration within and outside of the prostate can reduce the dosimetric coverage of the target volume and increase the dose to OARs (102). AI-based models can be a potential tool to resolve complications associated with marker-based techniques. Table 3 presents a summary of AI approaches to motion management in pelvic targets.

Table 3. Summary of publication using artificial intelligence for pelvic tumor tracking

Author	Year	Algorithm	Image Modality	No. Patients	Key findings in results
Zhao et al (103)	2019	DNN	CT	10 prostate cancer patients	Differences between the positions, predicted by DNN and ground truth positions are (mean \pm standard deviation) 1.58 ± 0.43 mm, 1.64 ± 0.43 mm, and 1.67 ± 0.36 mm in anterior-posterior, lateral, and oblique directions, respectively.
Zhu et al (104)	2019	Deep convolutional neural network	US	83 image pairs from 5 prostate cancer patients	CNN registration errors were < 5 mm in 81% of the cases. While manual registration errors were less than 5 mm in 61% of the cases. Also, advanced normalized correlation registration errors were < 5 mm only in 25% of the cases.
Mylonas et al (105)	2019	CNN(AlexNet)	kV X-ray	Training set (a phantom and 5 intrafraction images from three prostate cancer patients). Test set (12 fluoroscopic intrafraction images from 10 prostate cancer patients).	The method was effective for continuous fluoroscopic imaging where the markers were in the tracking window in subsequent image acquisition.
Amarsee et al (106)	2021	You Only Look Once (YOLO) convolutional neural network	kV X-ray	One phantom	The fiducial marker seeds were successfully detected in 98% of images from all gantry angles; the variation in the position of the seed center was within ± 1 mm. The percentage difference between the ground truth and the detected seeds was within 3%.
Fransson et al (98)	2021	Principal component analysis (PCA) (unsupervised machine learning)	MRI (MR-Linac)	9 healthy male volunteers	The cumulative variance of the eigenvalues from the PCA showed that 50% or more of the motion is explained in the first component for all subjects.
Nguyen et al (107)	2021	Kalman Filter framework	kV X-ray	17 prostate cancer patients (536 trajectories)	The maximum RMSE (without noise) was obtained at 0.4 ± 0.1 mm. With noise, the RMSE was 1.1 ± 0.1 mm.
Motley et al (102)	2022	You Only Look Once (YOLO)	kV X-ray	14 prostate cancer patients (~ 20,000 pelvis kV projection images)	The detection efficiency of the model was 96% with an RMSE of 0.3 pixels.
Chrystall et al (101)	2023	CNN	MV-based IGRT	29 prostate cancer patients	The AUC of 0.99, the sensitivity of 98.31%, and the specificity of 99.87% were achieved. The mean absolute geometric tracking error was 0.30 ± 0.27 for lateral and 0.35 ± 0.31 mm for SI directions of the MV images.

Tables 1-3 are not exhaustive; rather, representative publications are provided for illustration within each table. Studies covering several treatment sites are listed only once.

4. Artificial Intelligence for motion tracking in radiotherapy

4.1. Machine learning-based motion tracking

ML is a subfield of AI that utilizes algorithms to analyze input data and learn from them to provide recommendations and decisions. The typical workflow of classic ML includes data collection, data pre-processing, dataset (training, validation, and test) building, evaluation, and finally, deployment to production. In radiotherapy, classic ML methods can assist in analyzing different aspects of target motion to predict future positions and optimize treatment delivery. Several classic ML models have been proposed for tumor motion tracking. An ANN approach has been used in several studies to predict target position during treatment delivery. Isaksson *et al* (42) use the positions of external surrogate markers as an input for adaptive neural networks. The study demonstrated that the adaptive neural network provides a more accurate estimation of tumor position compared to fixed and adaptive linear filters. A subsequent study conducted by Murphy and Dieterich (44) confirmed the advantage of an adaptive neural network by comparing it against the linear adaptive filter. Krauss *et al* (52) performed a study on 12 samples of breathing data using linear regression (LR), kernel density estimation, SVM, and ANN. They indicated there were small differences between the models (Table 1). To improve the accuracy of ANN, some authors used an adaptive neuro-fuzzy inference system (ANFIS) which combines the benefit of both neural network and fuzzy logic systems (43, 50, 59). Kakar *et al*(43) used ANFIS to predict respiratory motion both more precisely and more quickly. Yan *et al*(45) developed a technique using ANN to predict tumor position by correlating the internal target position and an external surrogate. The proposed technique assumes a consistent correlation between internal and external movements, allowing for their prediction errors to be correlated with a linear model. In 2008, Cui *et al*(23) proposed that an SVM is a potentially accurate and efficient algorithm for predicting target position. Riaz *et al* (49) analyzed the performance of multi-dimensional adaptive filters versus a support vector machine (SVM) to predict lung tumor motion. They showed performance superior to the SVM model with RMSE < 2 mm at 1-second latency. Lin *et al* (48) further demonstrated the superiority of an ANN approach over SVM (Table 1). An extremely randomized tree (ERT) algorithm can also be used to predict tumor motion. Sakata *et al* (66) trained an ERT for position prediction of lung tumors using digitally reconstructed radiography (DRR) as inputs. They also used sliding window classification to provide a tumor likelihood map. The model was tested on 4DCT of eight patients and yielded an accuracy of 1.0 ± 0.3 mm (Table 1). In 2015, Bukovsky *et al* (58) presented a combination of quadratic neural unit (QNU) with modification of the Levenberg-Marquardt (L-M) algorithm to improve the accuracy of prediction. The authors achieved a prediction error of less than 1 mm on average of internal tumor position in total treatment time. Moreover, they indicated that QNU with the Levenberg-Marquardt (L-M) algorithm is faster and can yield more accurate results than multilayer perceptron (MLP). Whereas

a study conducted by Li *et al*(20) showed that the MLP model had better classification performance and stability for both lung and liver tumors compared to other models. The authors compared thirteen algorithms such as MLP, wide and deep (W&D), categorical boosting, light gradient boosting machine, extreme gradient boosting, adaptive boosting, random forest, decision tree, logistic regression via stochastic gradient descent, Gaussian Naive Bayes, SVM, linear support vector classifiers, and K-nearest neighbor. All models were developed based on radiomic features extracted from CT images of 108 patients with lung cancer and 71 patients with liver cancer. Stemkens *et al* (77) proposed a patient-specific method using a 3D motion model and fast 2D cine-MR imaging to estimate abdominal motion. The motion model was obtained by performing a principal component analysis (PCA) on inter-volume displacement vector fields (DVFs) that were derived from a pre-treatment 4D MRI scan.

The descriptions and drawbacks of common classic ML approaches are summarized in Table 4.

Table 4. A list of more common classic ML algorithms used for tumor tracking position.

Algorithm	Description	General Drawbacks
Artificial neural network (ANN)	A typical neural network has three layers including an input layer, a hidden layer, and an output layer. This system can process information and adjust to changing situations to optimize its performance in real time. It yields great accuracy for nonlinear and irregular patterns. It can be used for regression and classification. ANN includes MLP, QNU, Adaptive neuro-fuzzy inference system (ANFIS), Non-linear autoregressive with exogenous, wide, and deep (W&D)	Tend to overfit on small size datasets Memorize the training data and do not generalize well the learned knowledge to new or different data (108, 109)
Support vector machine (SVM)	The SVM is a supervised ML algorithm that performs classification and regression by finding the best line or decision boundaries to separate data into classes. The algorithm is a kernel-based model to solve linear and non-linear problems (110).	Strongly depends on the kernel Sensitive to noise Not suitable for large dataset
Decision Tree (DT)	The DT is a supervised ML algorithm that builds trees during training time over the entire dataset (111)	Sensitive to change It requires a relatively longer time to train the model (111)
Gaussian process regression (GPR)	The GPR is a probabilistic supervised ML algorithm to make predictions with uncertainty (112).	Their efficiency may decrease in high-dimensional spaces. The prediction is based on the entire sample/feature information (112)

4.2. Deep learning-based motion tracking

DL, a class of ML, uses a stack of processing layers with non-linear units that extract higher-level features from inputs. The advantage of DL over classic ML is that DL uses artificial neural networks to automatically learn from data and improve performance over time. The multilayered structure of DL enables it to self-train based on inputs and desired outputs (113). The workflow of DL is similar to classic ML and starts with data acquisition and preprocessing followed by building and training the model, optimization, evaluation, and predictions or inference. Recent advancements have increased interest in DL-based models for tracking target motion (Figure 1) and several algorithms have been trained for this task across most image modalities (Figure 3). In 2019, Zhao *et al* (103) conducted a study on 10 patients with prostate cancer who underwent either CBCT or orthogonal kV projections. The DL model used two networks: a region proposal network (RPN) and CNN. RPN was used to generate proposals for the region-based CNN to reduce computation time and enable real-time target detection. The two networks share all convolutional features. The study (Table 3) showed that highly accurate tumor localization can be achieved using CNN. However, Park *et al* (59) demonstrated that ANFIS was able to achieve an RMSE of 0.5 ± 0.8 mm using a 192.3 ms prediction, a 30.0% improvement over CNN. According to Park *et al*, the fuzzy logic component enhances the reasoning ability of the model when dealing with uncertainty (59). A study by Liang *et al.* (85) used an automated framework to evaluate intrafraction motion in CyberKnife X-ray images. The framework utilizes a fully convolutional network (FCN)-based module to detect fiducial markers and perform semantic segmentation using a U-Net architecture in full-size X-ray images. The 3D positions of the markers can then be reconstructed to evaluate intrafraction motion using a rigid transformation (Table 2). Wang *et al* (32) compared an LSTM approach against an SVM to estimate external respiratory motion and internal liver motion. The LSTM network was found to perform better on all planes. Edmunds *et al* (62) proposed to automatically segment the diaphragm using CBCT images for real-time tracking of lung tumors. A Mask R-CNN (Region Convolutional Neural Network) was trained on 3499 raw CBCT images from 10 patients with lung cancer. No manual intervention was required, and the model was able to track diaphragm motion in real time with a mean error of 4.4 mm. Several attempts were made to learn a joint mapping between partial views and 3D shapes. These efforts have established a path for connecting partial observations with high-dimensional data within a comprehensively trained deep framework. In 2020, Lei *et al* (7) proposed a novel method named TransNet including encoding, transformation, and decoding modules to draw 3D CT images from 2D projections. Later a fast volumetric imaging method with an orthogonal 2D kV/MV image pair using their modified deep learning method was developed for tumor localization in lung cancer radiation therapy (114). The result of this novel method (Table 1) suggests the feasibility and efficacy of the proposed technique to convert 2D to 3D images

which can be a potential solution for real-time lung tumor tracking in SBRT cases. The CT images were generated for one case by three different supervision strategies: 1) supervised by mean absolute error (MAE) and gradient difference (GD) losses (TransNet-v1); 2) supervised by MAE, GD, and perceptual losses (TransNet-v2); 3) supervised by a combination of MAE, GD, perceptual and adversarial losses (TransNet-v3). Figure 4 shows the volumetric image generation based on different X-ray projections acquired at different angles using TransNet-v3.

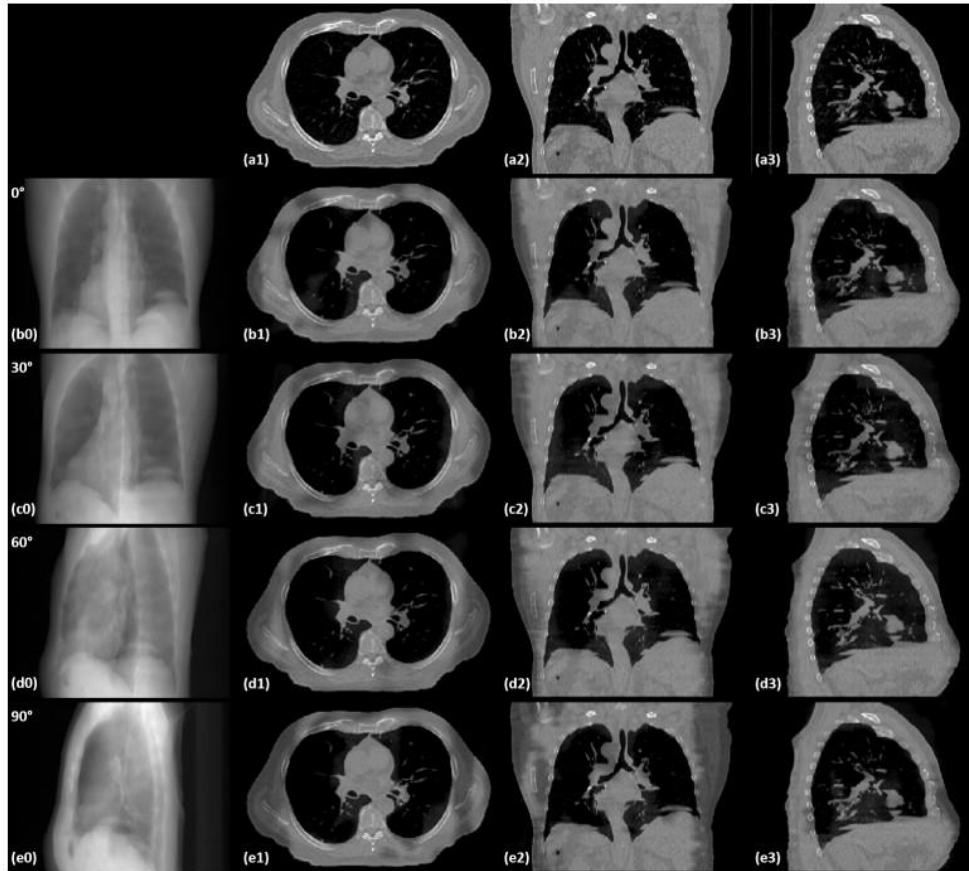


Figure 4. The 3D CT images are generated from a single 2D kV projection. (a1-a3) are ground truth 3D CT in axial, coronal, and sagittal views. Rows (b-d) demonstrate the projection data and corresponding generated 3D CT images for projection angles 0, 30, 60, and 90, respectively (7).

Liu *et al* (69) developed a new template network named NuTracker using an MLP comprising eight fully connected layers. The proposed model decomposes 4DCT images into template images and deformation fields using two coordinate-based neural networks to generate predictions from spatial coordinates and surrogate states. Hirai *et al* (64) trained a deep neural network (DNN) to generate a target probability map (TPM) to predict the position of lung and liver tumors. Crops of the target and surrounding anatomy were produced from DRR images. These crops were used to produce the TPM. Accuracy was quantified using

the Euclidian distance in 3D space between the calculated and reference tumor position (Table 1). US can provide real-time volumetric images to track intra-fraction motion during radiotherapy. Dai *et al* (67) implemented a generative adversarial Markov-like network (GAN-based Markov-like net) to estimate deformation vector fields (DVF) from sequential US frames. The positions of the landmarks in the untracked frames were determined by shifting landmarks in the tracked frame based on estimated DVFs (Figure 5). Zhang *et al.* (115) developed a cascade deep learning model with an attention network, a mask region-based convolutional neural network (mask R-CNN), and a long short-term memory (LSTM) network to track real-time liver motion in US image-guided radiation therapy.

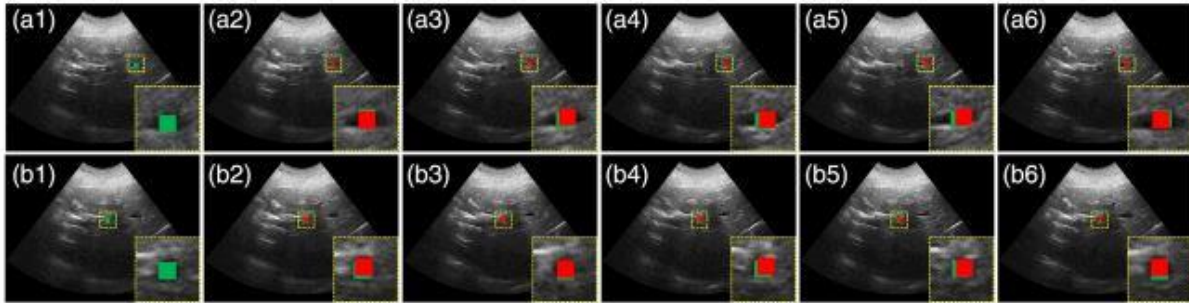


Figure 5. An illustrative example of 2D point-landmark tracking. *a1* and *b1* are ground truth and the location of ground truth landmarks are shown in green boxes. (*a2-a5*) and (*b2-b5*) are predicted locations and red boxes indicate the predicted landmark positions in the two different landmark tracking (67). (With permission)

5. Discussions

In the past, covering the target with large margins was required to compensate for intrafraction motion during radiotherapy, despite the risk of high-dose delivery to OARs. Techniques like tumor tracking or respiratory gating are now commonly used to maintain target coverage, but real-time monitoring is required to trigger beam on/off signals during gating (18). 4DCT/CBCT with implanted fiducial markers can aid real-time tracking of tumor positions; however, this invasive method introduces additional risk associated with possible procedure site infection, fiducial marker migration, non-trivial additional imaging dose exposure while increasing patient expense discomfort and inconvenience (116, 117). Furthermore, if fiducial markers are obscured by high-density material like bone, surgical clips, or stents, their value is significantly diminished (31). As a result, AI target motion tracking and prediction during radiotherapy to targets in the chest, abdomen, and pelvis, where SRS/SBRT are commonly used (Figure 2), may be useful (28, 29, 57, 60, 71, 95, 102, 106). The most popular classic ML algorithms for tumor tracking are NN and SVM algorithms (Tables 1-3). NN is of further interest due to its ability to capture both dynamic and structural phenomena, noise suppression, edge detection, and image enhancements (44, 58, 118). These features make it perhaps the best choice among other classic ML techniques for finding useful solutions

that require less human intervention. The SVM has been used widely due to its high performance, flexibility, and efficiency for small datasets (119). SVM is useful to deal with nonlinear classification based on a linear discriminant function in a high-dimensional (kernel) space (110). This feature improves its performance in processing nonlinear problems and real-time dynamic predictions (23, 32, 110).

5.1. Transition to Deep Learning

As illustrated in Figure 1, there has been a shift in AI-based motion-tracking research from ML to DL over the past decade. The drivers of this transition include the presence of large, high-quality, publicly available labeled datasets, along with the rapid advances in parallel graphic processing unit (GPU) computing, enabling more time-efficient computing and image analysis (62, 120). Before the emergence of powerful computers, CNNs, as a component of larger DL networks, required a significant amount of time to make predictions and provide results when using a central processing unit (CPU) (Table 1) (59). Classic ML techniques also require greater human input to achieve reasonable results, intrinsically introducing human error and bias that may influence a study's outcome (113). For instance, manual or semi-automated image segmentation, which is the primary step in data acquisition for training AI/ML algorithms, has several downsides. First, performing image segmentation manually is a time-consuming process, especially when too many images and datasets must be processed. Additionally, there is inherent user bias in manual and semi-automated segmentation, which can affect the robustness and reproducibility of extracted features. Also, in classical ML workflow the features are extracted manually from images and then classical ML models are built based on those features to categorize the object in the image. With DL, the extraction of the relevant features from images and modeling steps are automatic (113, 120). Compared with classic ML approaches, DL-based methods are more generalizable, as the same network and architecture used for one image modality can be applied to different pairs of image modalities with minimal adjustments (26, 34). This enables fast translation to multiple clinically useful imaging modalities. Unlike ML methods that tend to reach a plateau at a certain level of performance when more examples and training data are added to the network (121), DL networks often continue to improve as the size of data increases (113). DL-based methods have gained significant research and clinical interest in medical imaging generally and radiotherapy particularly due to these specific advantages.

5.2. Image modalities

Motion correction, before or during treatment, can be achieved with image-guided radiation therapy (IGRT). The integration of IGRT with clinical linear accelerators has improved patient care and quality of life. X-ray is the most common imaging modality employed in IGRT, primarily due to accessibility (Figure 3). X-ray use began with the use of megavoltage beam (MV) portal imaging. However, due to the poor

contrast resolution of MV images, in-room kV imaging systems were introduced. In kV images, soft-tissue contrast is higher, particularly when CBCT imaging is used. Planar kV (2D) and CBCT (3D) imaging are now typically available on modern standard-equipped linear accelerators. Motion-tracking systems equipped with IR-based monitoring may be used in conjunction with X-rays to further improve internal-external correlation (18). For example, the CyberKnife Synchrony system utilizes stereoscopic X-ray imaging to detect implanted clips and correlate them with external surrogates (50). Varian TrueBeam linear accelerators can also use respiratory gating and on-board kV imaging to verify internal target anatomy at the start of the gated treatment window, guided by the RPM signal (18). MRI is the second most common imaging modality in clinical practice due to the integration of MR imaging with commercially available linear accelerators. The introduction of the MRI-linear accelerator (MR-linac) enables imaging both before and during treatment with greater soft tissue contrast relative to X-rays, making it easier to differentiate targets from normal tissue (98). Notably, MR-linac does not require the implantation of fiducial markers or the delivery of extra doses to the patient. However, its use is limited by the size of the imaging bore and is contraindicated in the presence of ferrous metal implants or cardiac pacemakers/defibrillators. US imaging is another well-established imaging technique that can provide real-time volumetric images to track intra-fraction motion without ionizing radiation (82). Yet, due to the poor penetration of US waves into deeper tissues, US cannot be used reliably in clinically important regions such as the skull and thorax (122).

Despite the many advantages of IGRT, limitations remain. X-ray-based kV and specifically MV imaging reliably capture osseous anatomy but fail in effectively resolving tumor motion within soft tissues (123). CBCT, which may be used to acquire a volumetric image of the patient's anatomy before treatment, cannot be used during treatment delivery. Regardless, CBCT is prone to severe artifacts, including streaking, beam hardening, and aliasing as well as those due to motion, which severely degrade image quality (124). While 4DCT represents a meaningful technological advance in the delivery of radiation therapy, it cannot provide information on variations between breathing cycles or variations occurring on a time scale beyond a magnitude of seconds (125). AI-based techniques have shown great potential to address this question of how information—or lack thereof—collected during IGRT can be used in real-time motion management (Tables 2-4).

5.3.Current Limitations and Potential Solutions

Despite the proliferation of AI-based solutions in the healthcare setting, efforts toward standardization and regulation are lacking (126, 127). Many AI techniques fail to meet expectations for clinical utility, requiring significant time or computing resources to complete complex calculations. Additionally, the presence of bias in human-led data collection and model training, coupled with a lack of standardized

reporting for research and clinical validation results makes it difficult to reproducibly apply these techniques in practice (128).

Furthermore, trained algorithms often fail when applied to different datasets due to limited generalization (resulting from small and homogeneous training data sets) (121, 129). Tables 2-4 indicate that some early studies had a limited number of patients, resulting in inadequate patient datasets for systematic analysis of intrafraction motion. Small sample sizes can produce false-negative results (130) and may yield falsely higher accuracy due to overfitting or random effects (121, 131). Ultimately, the limited size of the training and test sets introduces bias and increases variance in model performance (113, 119). To resolve this issue, many follow Cohen's equations (132) to determine the effect size by calculating the mean and variance. However, there are two methods to calculate the variance: a) population variance, and b) sample variance. To calculate population variance, all data is needed whereas for computing sample variance we only need a portion of it. This difference in variance calculation can affect the outcome of these measurements. Rajput *et al* (121) proposed a new method to evaluate sample size using effect sizes (average and grand) and ML to resolve this issue.

AI results are further influenced by hardware specifications and imaging protocols, in addition to variability between individual patients such as anatomic geometry, and tumor location. The impact of such variations commonly limits model accuracy and generalizability (133-135). Many AI studies lack transparency in feature selection, training, validation, and testing: even sample sizes often go unreported by many authors. To address these problems, a comprehensive guideline for the evaluation and development of reliable AI models in medical imaging (Checklist for Artificial Intelligence in Medical Imaging, CLAIM), has been proposed by Mongan et al. (129). The CLAIM framework details 42 items guide authors and reviewers of AI manuscripts by providing recommendations on generalizability and reproducibility for frequently encountered tasks like classification, image reconstruction, image analysis, and workflow optimization. Improved CLAIM adherence could enhance the robustness and generalizability of trained algorithms to boost the adoption of AI in clinical practice and accelerate investigators' progress toward future innovation.

5.4.Future Direction

There are currently fewer research papers focusing on AI for monitoring intrafraction motion in radiotherapy compared to other AI applications, such as automatic segmentation. Moreover, current AI methods are hindered by high latency due to slow processing speed. However, with further advancements in hardware and software design, it is expected that a linear accelerator equipped for standard IGRT may

be used in the near future to monitor the intrafraction motion of radiotherapy targets without additional hardware.

6. Conclusion

The use of AI in motion monitoring during radiotherapy has demonstrated significant success in improving accuracy compared to conventional techniques. AI methods have shown potential in markerless tracking of intrafraction movements by enhancing target visibility within onboard projection images. Although AI networks can provide accurate predictions, their decisions can be difficult to interpret, explain, debug, and validate, which poses a regulatory and ethical challenge. More research on intrafraction motion management is needed to reliably evaluate the performance of proposed AI methods.

Acknowledgement

This research is funded by the National Cancer Institute under Award Number R01CA272991, and National Institute of Biomedical Imaging and Bioengineering under Award Number R56EB033332.

Disclosures

The authors declare no conflicts of interest.

5. Reference:

1. Parsai EI, Pearson D, Kvale T. Consequences of removing the flattening filter from linear accelerators in generating high dose rate photon beams for clinical applications: A Monte Carlo study verified by measurement. *Nuclear Instruments and Methods in Physics Research Section B: Beam Interactions with Materials and Atoms*. 2007;261(1):755-9.
2. Ghemiş DM, Marcu LG. Progress and prospects of flattening filter free beam technology in radiosurgery and stereotactic body radiotherapy. *Critical Reviews in Oncology/Hematology*. 2021;163:103396.
3. Lai Y, Chen S, Xu C, Shi L, Fu L, Ha H, et al. Dosimetric superiority of flattening filter free beams for single-fraction stereotactic radiosurgery in single brain metastasis. *Oncotarget*. 2017;8(21):35272-9.
4. Mamballikalam G, Senthilkumar S, Clinto CO, Ahamed Basith PM, Jaon Bos RC, Thomas T. Time motion study to evaluate the impact of flattening filter free beam on overall treatment time for frameless intracranial radiosurgery using Varian TrueBeam((R)) linear accelerator. *Rep Pract Oncol Radiother*. 2021;26(1):111-8.
5. Lovelock DM, Messineo AP, Cox BW, Kollmeier MA, Zelefsky MJ. Continuous monitoring and intrafraction target position correction during treatment improves target coverage for patients undergoing SBRT prostate therapy. *Int J Radiat Oncol Biol Phys*. 2015;91(3):588-94.
6. Fast M, van de Schoot A, van de Lindt T, Carbaat C, van der Heide U, Sonke JJ. Tumor Trailing for Liver SBRT on the MR-Linac. *Int J Radiat Oncol Biol Phys*. 2019;103(2):468-78.
7. Lei Y, Tian Z, Wang T, Higgins K, Bradley JD, Curran WJ, et al. Deep learning-based real-time volumetric imaging for lung stereotactic body radiation therapy: a proof of concept study. *Phys Med Biol*. 2020;65(23):235003.
8. Han B, Wu B, Hu F, Ma Y, Wang H, Han X, et al. Simulation of dosimetric consequences of intrafraction variation of tumor drift in lung cancer stereotactic body radiotherapy. *Frontiers in Oncology*. 2022;12.
9. Boda-Heggemann J, Köhler FM, Wertz H, Ehmann M, Hermann B, Riesenacker N, et al. Intrafraction motion of the prostate during an IMRT session: a fiducial-based 3D measurement with Cone-beam CT. *Radiation Oncology*. 2008;3(1):37.

10. Poulsen PR, Worm ES, Hansen R, Larsen LP, Grau C, Høyer M. Respiratory gating based on internal electromagnetic motion monitoring during stereotactic liver radiation therapy: First results. *Acta Oncol.* 2015;54(9):1445-52.
11. Tacke MB, Nill S, Krauss A, Oelfke U. Real-time tumor tracking: automatic compensation of target motion using the Siemens 160 MLC. *Med Phys.* 2010;37(2):753-61.
12. Jöhl A, Ehrbar S, Guckenberger M, Klöck S, Mack A, Meboldt M, et al. The ideal couch tracking system—Requirements and evaluation of current systems. *Journal of Applied Clinical Medical Physics.* 2019;20(10):152-9.
13. Bottero M, Dipasquale G, Lancia A, Miralbell R, Jaccard M, Zilli T. Electromagnetic Transponder Localization and Real-Time Tracking for Prostate Cancer Radiation Therapy: Clinical Impact of Metallic Hip Prostheses. *Practical Radiation Oncology.* 2020;10(6):e538-e42.
14. Boggs DH, Popple R, McDonald A, Minnich D, Willey CD, Spencer S, et al. Electromagnetic Transponder Based Tracking and Gating in the Radiotherapeutic Treatment of Thoracic Malignancies. *Pract Radiat Oncol.* 2019;9(6):456-64.
15. Zollner B, Heinz C, Pitzler S, Manapov F, Kantz S, Rottler MC, et al. Stereoscopic X-ray imaging, cone beam CT, and couch positioning in stereotactic radiotherapy of intracranial tumors: preliminary results from a cross-modality pilot installation. *Radiation Oncology.* 2016;11(1):158.
16. Lyatskaya Y, Lu HM, Chin L. Performance and characteristics of an IR localizing system for radiation therapy. *J Appl Clin Med Phys.* 2006;7(2):18-37.
17. Western C, Hristov D, Schlosser J. Ultrasound Imaging in Radiation Therapy: From Interfractional to Intrafractional Guidance. *Cureus.* 2015;7(6):e280.
18. Bertholet J, Knopf A, Eiben B, McClelland J, Grimwood A, Harris E, et al. Real-time intrafraction motion monitoring in external beam radiotherapy. *Phys Med Biol.* 2019;64(15):15tr01.
19. Wu VWC, Ng APL, Cheung EKW. Intrafractional motion management in external beam radiotherapy. *J Xray Sci Technol.* 2019;27(6):1071-86.
20. Li G, Zhang X, Song X, Duan L, Wang G, Xiao Q, et al. Machine learning for predicting accuracy of lung and liver tumor motion tracking using radiomic features. *Quant Imaging Med Surg.* 2023;13(3):1605-18.

21. Zhang X, Song X, Li G, Duan L, Wang G, Dai G, et al. Machine Learning Radiomics Model for External and Internal Respiratory Motion Correlation Prediction in Lung Tumor. *Technol Cancer Res Treat*. 2022;21:15330338221143224.
22. Yun J, Mackenzie M, Rathee S, Robinson D, Fallone BG. An artificial neural network (ANN)-based lung-tumor motion predictor for intrafractional MR tumor tracking. *Med Phys*. 2012;39(7):4423-33.
23. Cui Y, Dy JG, Alexander B, Jiang SB. Fluoroscopic gating without implanted fiducial markers for lung cancer radiotherapy based on support vector machines. *Phys Med Biol*. 2008;53(16):N315-27.
24. Lin H, Zou W, Li T, Feigenberg SJ, Teo BK, Dong L. A Super-Learner Model for Tumor Motion Prediction and Management in Radiation Therapy: Development and Feasibility Evaluation. *Sci Rep*. 2019;9(1):14868.
25. Mori S. Deep architecture neural network-based real-time image processing for image-guided radiotherapy. *Phys Med*. 2017;40:79-87.
26. Terpstra ML, Maspero M, Bruijnen T, Verhoeff JJC, Lagendijk JJW, van den Berg CAT. Real-time 3D motion estimation from undersampled MRI using multi-resolution neural networks. *Med Phys*. 2021;48(11):6597-613.
27. Teo PT, Bajaj A, Randall J, Lou B, Shah J, Gopalakrishnan M, et al. Deterministic small-scale undulations of image-based risk predictions from the deep learning of lung tumors in motion. *Med Phys*. 2022;49(11):7347-56.
28. Pohl M, Uesaka M, Demachi K, Bhusal Chhatkuli R. Prediction of the motion of chest internal points using a recurrent neural network trained with real-time recurrent learning for latency compensation in lung cancer radiotherapy. *Comput Med Imaging Graph*. 2021;91:101941.
29. Momin S, Lei Y, Tian Z, Wang T, Roper J, Kesarwala AH, et al. Lung tumor segmentation in 4D CT images using motion convolutional neural networks. *Med Phys*. 2021;48(11):7141-53.
30. Bharadwaj S, Prasad S, Almekkawy M. An Upgraded Siamese Neural Network for Motion Tracking in Ultrasound Image Sequences. *IEEE Trans Ultrason Ferroelectr Freq Control*. 2021;68(12):3515-27.

31. Ahmed AM, Gargett M, Madden L, Mylonas A, Chrystall D, Brown R, et al. Evaluation of deep learning based implanted fiducial markers tracking in pancreatic cancer patients. *Biomed Phys Eng Express*. 2023;9(3).
32. Wang G, Li Z, Li G, Dai G, Xiao Q, Bai L, et al. Real-time liver tracking algorithm based on LSTM and SVR networks for use in surface-guided radiation therapy. *Radiat Oncol*. 2021;16(1):13.
33. Ma Y, Mao J, Liu X, Dai Z, Zhang H, Zhang X, et al. Deep learning-based internal gross target volume definition in 4D CT images of lung cancer patients. *Med Phys*. 2023;50(4):2303-16.
34. Wang T, Lei Y, Fu Y, Wynne JF, Curran WJ, Liu T, et al. A review on medical imaging synthesis using deep learning and its clinical applications. *J Appl Clin Med Phys*. 2021;22(1):11-36.
35. Page MJ, McKenzie JE, Bossuyt PM, Boutron I, Hoffmann TC, Mulrow CD, et al. The PRISMA 2020 statement: An updated guideline for reporting systematic reviews. *PLOS Medicine*. 2021;18(3):e1003583.
36. Siegel RL, Miller KD, Fuchs HE, Jemal A. Cancer statistics, 2022. *CA Cancer J Clin*. 2022;72(1):7-33.
37. Huang Y, Dong Z, Wu H, Li C, Liu H, Zhang Y. Deep learning-based synthetization of real-time in-treatment 4D images using surface motion and pretreatment images: A proof-of-concept study. *Med Phys*. 2022;49(11):7016-24.
38. Molitoris JK, Diwanji T, Snider JW, 3rd, Mossahebi S, Samanta S, Badiyan SN, et al. Advances in the use of motion management and image guidance in radiation therapy treatment for lung cancer. *J Thorac Dis*. 2018;10(Suppl 21):S2437-S50.
39. Cole AJ, Hanna GG, Jain S, O'Sullivan JM. Motion management for radical radiotherapy in non-small cell lung cancer. *Clin Oncol (R Coll Radiol)*. 2014;26(2):67-80.
40. Hohenforst-Schmidt W, Zarogoulidis P, Vogl T, Turner JF, Browning R, Linsmeier B, et al. Cone Beam Computertomography (CBCT) in Interventional Chest Medicine - High Feasibility for Endobronchial Realtime Navigation. *J Cancer*. 2014;5(3):231-41.
41. Liu H, Chen R, Tong C, Liang XW. MRI versus CT for the detection of pulmonary nodules: A meta-analysis. *Medicine (Baltimore)*. 2021;100(42):e27270.

42. Isaksson M, Jalden J, Murphy MJ. On using an adaptive neural network to predict lung tumor motion during respiration for radiotherapy applications. *Med Phys*. 2005;32(12):3801-9.
43. Kakar M, Nyström H, Aarup LR, Nøttrup TJ, Olsen DR. Respiratory motion prediction by using the adaptive neuro fuzzy inference system (ANFIS). *Physics in Medicine & Biology*. 2005;50(19):4721.
44. Murphy MJ, Dieterich S. Comparative performance of linear and nonlinear neural networks to predict irregular breathing. *Phys Med Biol*. 2006;51(22):5903-14.
45. Yan H, Yin FF, Zhu GP, Ajlouni M, Kim JH. Adaptive prediction of internal target motion using external marker motion: a technical study. *Phys Med Biol*. 2006;51(1):31-44.
46. Zhang Q, Pevsner A, Hertanto A, Hu YC, Rosenzweig KE, Ling CC, et al. A patient-specific respiratory model of anatomical motion for radiation treatment planning. *Med Phys*. 2007;34(12):4772-81.
47. Lin T, Cervino LI, Tang X, Vasconcelos N, Jiang SB. Fluoroscopic tumor tracking for image-guided lung cancer radiotherapy. *Phys Med Biol*. 2009;54(4):981-92.
48. Lin T, Li R, Tang X, Dy JG, Jiang SB. Markerless gating for lung cancer radiotherapy based on machine learning techniques. *Phys Med Biol*. 2009;54(6):1555-63.
49. Riaz N, Shanker P, Wiersma R, Gudmundsson O, Mao W, Widrow B, et al. Predicting respiratory tumor motion with multi-dimensional adaptive filters and support vector regression. *Phys Med Biol*. 2009;54(19):5735-48.
50. Torshabi AE, Pella A, Riboldi M, Baroni G. Targeting accuracy in real-time tumor tracking via external surrogates: a comparative study. *Technol Cancer Res Treat*. 2010;9(6):551-62.
51. Cervino LI, Du J, Jiang SB. MRI-guided tumor tracking in lung cancer radiotherapy. *Phys Med Biol*. 2011;56(13):3773-85.
52. Krauss A, Nill S, Oelfke U. The comparative performance of four respiratory motion predictors for real-time tumour tracking. *Phys Med Biol*. 2011;56(16):5303-17.
53. Li R, Lewis JH, Jia X, Zhao T, Liu W, Wuenschel S, et al. On a PCA-based lung motion model. *Phys Med Biol*. 2011;56(18):6009-30.
54. Fayad H, Pan T, Pradier O, Visvikis D. Patient specific respiratory motion modeling using a 3D patient's external surface. *Med Phys*. 2012;39(6):3386-95.

55. Li G, Wei J, Huang H, Gaebler CP, Yuan A, Deasy JO. Automatic assessment of average diaphragm motion trajectory from 4DCT images through machine learning. *Biomed Phys Eng Express*. 2015;1(4).
56. Bukhari W, Hong SM. Real-time prediction and gating of respiratory motion using an extended Kalman filter and Gaussian process regression. *Phys Med Biol*. 2015;60(1):233-52.
57. Yun J, Yip E, Gabos Z, Wachowicz K, Rathee S, Fallone BG. Neural-network based autocontouring algorithm for intrafractional lung-tumor tracking using Linac-MR. *Med Phys*. 2015;42(5):2296-310.
58. Bukovsky I, Homma N, Ichiji K, Cejnek M, Slama M, Benes PM, et al. A fast neural network approach to predict lung tumor motion during respiration for radiation therapy applications. *Biomed Res Int*. 2015;2015:489679.
59. Park S, Lee SJ, Weiss E, Motai Y. Intra- and Inter-Fractional Variation Prediction of Lung Tumors Using Fuzzy Deep Learning. *IEEE J Transl Eng Health Med*. 2016;4:4300112.
60. Teo TP, Ahmed SB, Kawalec P, Alayoubi N, Bruce N, Lyn E, et al. Feasibility of predicting tumor motion using online data acquired during treatment and a generalized neural network optimized with offline patient tumor trajectories. *Med Phys*. 2018;45(2):830-45.
61. Terunuma T, Tokui A, Sakae T. Novel real-time tumor-contouring method using deep learning to prevent mistracking in X-ray fluoroscopy. *Radiol Phys Technol*. 2018;11(1):43-53.
62. Edmunds D, Sharp G, Winey B. Automatic diaphragm segmentation for real-time lung tumor tracking on cone-beam CT projections: a convolutional neural network approach. *Biomed Phys Eng Express*. 2019;5(3).
63. Jiang K, Fujii F, Shiinoki T. Prediction of lung tumor motion using nonlinear autoregressive model with exogenous input. *Phys Med Biol*. 2019;64(21):21NT02.
64. Hirai R, Sakata Y, Tanizawa A, Mori S. Real-time tumor tracking using fluoroscopic imaging with deep neural network analysis. *Phys Med*. 2019;59:22-9.
65. Mori S, Hirai R, Sakata Y. Simulated four-dimensional CT for markerless tumor tracking using a deep learning network with multi-task learning. *Phys Med*. 2020;80:151-8.
66. Sakata Y, Hirai R, Kobuna K, Tanizawa A, Mori S. A machine learning-based real-time tumor tracking system for fluoroscopic gating of lung radiotherapy. *Phys Med Biol*. 2020;65(8):085014.

67. Dai X, Lei Y, Roper J, Chen Y, Bradley JD, Curran WJ, et al. Deep learning-based motion tracking using ultrasound images. *Med Phys*. 2021;48(12):7747-56.
68. He X, Cai W, Li F, Fan Q, Zhang P, Cuaron JJ, et al. Decompose kV projection using neural network for improved motion tracking in paraspinal SBRT. *Med Phys*. 2021;48(12):7590-601.
69. Liu C, Wang Q, Si W, Ni X. NuTracker: a coordinate-based neural network representation of lung motion for intrafraction tumor tracking with various surrogates in radiotherapy. *Phys Med Biol*. 2022;68(1).
70. Lombardo E, Rabe M, Xiong Y, Nierer L, Cusumano D, Placidi L, et al. Offline and online LSTM networks for respiratory motion prediction in MR-guided radiotherapy. *Phys Med Biol*. 2022;67(9).
71. Hindley N, Shieh CC, Keall P. A patient-specific deep learning framework for 3D motion estimation and volumetric imaging during lung cancer radiotherapy. *Phys Med Biol*. 2023;68(14).
72. Huttinga NRF, Akdag O, Fast MF, Verhoeff JJC, Mohamed Hoesein FAA, van den Berg CAT, et al. Real-time myocardial landmark tracking for MRI-guided cardiac radio-ablation using Gaussian Processes. *Phys Med Biol*. 2023;68(14).
73. Lombardo E, Rabe M, Xiong Y, Nierer L, Cusumano D, Placidi L, et al. Evaluation of real-time tumor contour prediction using LSTM networks for MR-guided radiotherapy. *Radiother Oncol*. 2023;182:109555.
74. Zhou D, Nakamura M, Mukumoto N, Matsuo Y, Mizowaki T. Feasibility study of deep learning-based markerless real-time lung tumor tracking with orthogonal X-ray projection images. *J Appl Clin Med Phys*. 2023;24(4):e13894.
75. Abbas H, Chang B, Chen ZJ. Motion management in gastrointestinal cancers. *J Gastrointest Oncol*. 2014;5(3):223-35.
76. Gou S, Lee P, Hu P, Rwigema JC, Sheng K. Feasibility of automated 3-dimensional magnetic resonance imaging pancreas segmentation. *Adv Radiat Oncol*. 2016;1(3):182-93.
77. Stemkens B, Tijssen RH, de Senneville BD, Lagendijk JJ, van den Berg CA. Image-driven, model-based 3D abdominal motion estimation for MR-guided radiotherapy. *Phys Med Biol*. 2016;61(14):5335-55.

78. Ozkan E, Tanner C, Kastelic M, Mattausch O, Makhinya M, Goksel O. Robust motion tracking in liver from 2D ultrasound images using supporters. *Int J Comput Assist Radiol Surg.* 2017;12(6):941-50.
79. Grabner H, Matas J, Gool LV, Cattin P, editors. *Tracking the invisible: Learning where the object might be.* 2010 IEEE Computer Society Conference on Computer Vision and Pattern Recognition; 2010 13-18 June 2010.
80. Dick D, Wu X, Hatoum GF, Zhao W. A fiducial-less tracking method for radiation therapy of liver tumors by diaphragm disparity analysis part 1: simulation study using machine learning through artificial neural network. *Journal of Radiation Oncology.* 2018;7(3):275-84.
81. Dick D, Wu X, Hatoum GF, Zhao W. A fiducial-less tracking method for radiation therapy of liver tumors by diaphragm disparity analysis part 2: validation study by using clinical data. *Journal of Radiation Oncology.* 2018;7(4):345-56.
82. Huang P, Su L, Chen S, Cao K, Song Q, Kazanzides P, et al. 2D ultrasound imaging based intra-fraction respiratory motion tracking for abdominal radiation therapy using machine learning. *Phys Med Biol.* 2019;64(18):185006.
83. Huang P, Yu G, Lu H, Liu D, Xing L, Yin Y, et al. Attention-aware fully convolutional neural network with convolutional long short-term memory network for ultrasound-based motion tracking. *Med Phys.* 2019;46(5):2275-85.
84. Zhao W, Shen L, Han B, Yang Y, Cheng K, Toesca DAS, et al. Markerless Pancreatic Tumor Target Localization Enabled By Deep Learning. *Int J Radiat Oncol Biol Phys.* 2019;105(2):432-9.
85. Liang Z, Zhou Q, Yang J, Zhang L, Liu D, Tu B, et al. Artificial intelligence-based framework in evaluating intrafraction motion for liver cancer robotic stereotactic body radiation therapy with fiducial tracking. *Med Phys.* 2020;47(11):5482-9.
86. Liu M, Cygler JE, Vandervoort E. Patient-specific PTV margins for liver stereotactic body radiation therapy determined using support vector classification with an early warning system for margin adaptation. *Med Phys.* 2020;47(10):5172-82.
87. Roggen T, Bobic M, Givehchi N, Scheib SG. Deep Learning model for markerless tracking in spinal SBRT. *Phys Med.* 2020;74:66-73.

88. Terpstra ML, Maspero M, d'Agata F, Stemkens B, Intven MPW, Lagendijk JJW, et al. Deep learning-based image reconstruction and motion estimation from undersampled radial k-space for real-time MRI-guided radiotherapy. *Phys Med Biol.* 2020;65(15):155015.
89. Romaguera LV, Mezheritsky T, Mansour R, Carrier JF, Kadoury S. Probabilistic 4D predictive model from in-room surrogates using conditional generative networks for image-guided radiotherapy. *Med Image Anal.* 2021;74:102250.
90. Shao HC, Huang X, Folkert MR, Wang J, Zhang Y. Automatic liver tumor localization using deep learning-based liver boundary motion estimation and biomechanical modeling (DL-Bio). *Med Phys.* 2021;48(12):7790-805.
91. He X, Cai W, Li F, Zhang P, Reyngold M, Cuaron JJ, et al. Automatic stent recognition using perceptual attention U-net for quantitative intrafraction motion monitoring in pancreatic cancer radiotherapy. *Med Phys.* 2022;49(8):5283-93.
92. Liu L, Shen L, Johansson A, Balter JM, Cao Y, Chang D, et al. Real time volumetric MRI for 3D motion tracking via geometry-informed deep learning. *Med Phys.* 2022;49(9):6110-9.
93. Shao HC, Li T, Dohopolski MJ, Wang J, Cai J, Tan J, et al. Real-time MRI motion estimation through an unsupervised k-space-driven deformable registration network (KS-RegNet). *Phys Med Biol.* 2022;67(13).
94. Shao HC, Wang J, Bai T, Chun J, Park JC, Jiang S, et al. Real-time liver tumor localization via a single x-ray projection using deep graph neural network-assisted biomechanical modeling. *Phys Med Biol.* 2022;67(11).
95. Dai Z, He Q, Zhu L, Zhang B, Jin H, Yang G, et al. Automatic prediction model for online diaphragm motion tracking based on optical surface monitoring by machine learning. *Quant Imaging Med Surg.* 2023;13(4):2065-80.
96. Hunt B, Gill GS, Alexander DA, Streeter SS, Gladstone DJ, Russo GA, et al. Fast Deformable Image Registration for Real-Time Target Tracking During Radiation Therapy Using Cine MRI and Deep Learning. *Int J Radiat Oncol Biol Phys.* 2023;115(4):983-93.
97. Shao HC, Li Y, Wang J, Jiang SB, Zhang Y. Real-time liver tumor localization via combined surface imaging and a single x-ray projection. *Phys Med Biol.* 2023.

98. Fransson S, Tilly D, Ahnesjö A, Nyholm T, Strand R. Intrafractional motion models based on principal components in Magnetic Resonance guided prostate radiotherapy. *Phys Imaging Radiat Oncol.* 2021;20:17-22.
99. Oehler C, Roehner N, Sumila M, Curschmann J, Storelli F, Zwahlen DR, et al. Intrafraction Prostate Motion Management for Ultra-Hypofractionated Radiotherapy of Prostate Cancer. *Curr Oncol.* 2022;29(9):6314-24.
100. Tong X, Chen X, Li J, Xu Q, Lin MH, Chen L, et al. Intrafractional prostate motion during external beam radiotherapy monitored by a real-time target localization system. *J Appl Clin Med Phys.* 2015;16(2):5013.
101. Chrystall D, Mylonas A, Hewson E, Martin J, Keall P, Booth J, et al. Deep learning enables MV-based real-time image guided radiation therapy for prostate cancer patients. *Phys Med Biol.* 2023;68(9).
102. Motley R, Ramachandran P, Fielding A. A feasibility study on the development and use of a deep learning model to automate real-time monitoring of tumor position and assessment of interfraction fiducial marker migration in prostate radiotherapy patients(). *Biomed Phys Eng Express.* 2022;8(3).
103. Zhao W, Han B, Yang Y, Buyyounouski M, Hancock SL, Bagshaw H, et al. Incorporating imaging information from deep neural network layers into image guided radiation therapy (IGRT). *Radiother Oncol.* 2019;140:167-74.
104. Zhu N, Najafi M, Han B, Hancock S, Hristov D. Feasibility of Image Registration for Ultrasound-Guided Prostate Radiotherapy Based on Similarity Measurement by a Convolutional Neural Network. *Technol Cancer Res Treat.* 2019;18:1533033818821964.
105. Mylonas A, Keall PJ, Booth JT, Shieh CC, Eade T, Poulsen PR, et al. A deep learning framework for automatic detection of arbitrarily shaped fiducial markers in intrafraction fluoroscopic images. *Med Phys.* 2019;46(5):2286-97.
106. Amarsee K, Ramachandran P, Fielding A, Lehman M, Noble C, Perrett B, et al. Automatic Detection and Tracking of Marker Seeds Implanted in Prostate Cancer Patients using a Deep Learning Algorithm. *J Med Phys.* 2021;46(2):80-7.
107. Nguyen DT, Keall P, Booth J, Shieh CC, Poulsen P, O'Brien R. A real-time IGRT method using a Kalman filter framework to extract 3D positions from 2D projections. *Phys Med Biol.* 2021;66(21).

108. Malekian A, Chitsaz N. Chapter 4 - Concepts, procedures, and applications of artificial neural network models in streamflow forecasting. In: Sharma P, Machiwal D, editors. *Advances in Streamflow Forecasting*; Elsevier; 2021. p. 115-47.
109. Park YS, Lek S. Chapter 7 - Artificial Neural Networks: Multilayer Perceptron for Ecological Modeling. In: Jørgensen SE, editor. *Developments in Environmental Modelling*. 28: Elsevier; 2016. p. 123-40.
110. Suthaharan S. Support Vector Machine. In: Suthaharan S, editor. *Machine Learning Models and Algorithms for Big Data Classification: Thinking with Examples for Effective Learning*. Boston, MA: Springer US; 2016. p. 207-35.
111. L. Breiman, J. Friedman, R. Olshen, Stone. C. *Classification and Regression Trees*. *Classification and Regression Trees (Wadsworth Statistics/Probability)* 1ed: Routledge; 1984. p. 246-80.
112. Seeger M. Gaussian processes for machine learning. *Int J Neural Syst*. 2004;14(2):69-106.
113. Castiglioni I, Rundo L, Codari M, Di Leo G, Salvatore C, Interlenghi M, et al. AI applications to medical images: From machine learning to deep learning. *Phys Med*. 2021;83:9-24.
114. Lei Y, Tian Z, Wang T, Roper J, Xie H, Kesarwala AH, et al. Deep learning-based fast volumetric imaging using kV and MV projection images for lung cancer radiotherapy: A feasibility study. *Med Phys*. 2023;50(9):5518-27.
115. Zhang Y, Dai X, Tian Z, Lei Y, Wynne JF, Patel P, et al. Landmark tracking in liver US images using cascade convolutional neural networks with long short-term memory. *Meas Sci Technol*. 2023;34(5):054002.
116. O'Neill AG, Jain S, Hounsell AR, O'Sullivan JM. Fiducial marker guided prostate radiotherapy: a review. *Br J Radiol*. 2016;89(1068):20160296.
117. Khullar K, Dhawan ST, Nosher J, Jabbour SK. Fiducial marker migration following computed tomography-guided placement in the liver: a case report. *AME Case Rep*. 2021;5:15.
118. Egmont-Petersen M, de Ridder D, Handels H. Image processing with neural networks—a review. *Pattern Recognition*. 2002;35(10):2279-301.
119. Way TW, Sahiner B, Hadjiiski LM, Chan H-P. Effect of finite sample size on feature selection and classification: A simulation study. *Medical Physics*. 2010;37(2):907-20.

120. Chai J, Zeng H, Li A, Ngai EWT. Deep learning in computer vision: A critical review of emerging techniques and application scenarios. *Machine Learning with Applications*. 2021;6:100134.
121. Rajput D, Wang WJ, Chen CC. Evaluation of a decided sample size in machine learning applications. *BMC Bioinformatics*. 2023;24(1):48.
122. Klibanov AL, Hossack JA. Ultrasound in Radiology: From Anatomic, Functional, Molecular Imaging to Drug Delivery and Image-Guided Therapy. *Invest Radiol*. 2015;50(9):657-70.
123. Fung AY, Grimm SY, Wong JR, Uematsu M. Computed tomography localization of radiation treatment delivery versus conventional localization with bony landmarks. *J Appl Clin Med Phys*. 2003;4(2):112-9.
124. van Timmeren JE, Leijenaar RTH, van Elmpt W, Reymen B, Oberije C, Monshouwer R, et al. Survival prediction of non-small cell lung cancer patients using radiomics analyses of cone-beam CT images. *Radiotherapy and Oncology*. 2017;123(3):363-9.
125. Korreman SS. Image-guided radiotherapy and motion management in lung cancer. *Br J Radiol*. 2015;88(1051):20150100.
126. Chua IS, Gazieli-Yablowitz M, Korach ZT, Kehl KL, Levitan NA, Arriaga YE, et al. Artificial intelligence in oncology: Path to implementation. *Cancer Med*. 2021;10(12):4138-49.
127. Ngiam KY, Khor IW. Big data and machine learning algorithms for health-care delivery. *Lancet Oncol*. 2019;20(5):e262-e73.
128. Chalkidou A, O'Doherty MJ, Marsden PK. False Discovery Rates in PET and CT Studies with Texture Features: A Systematic Review. (1932-6203 (Electronic)).
129. Mongan J, Moy L, Kahn CE, Jr. Checklist for Artificial Intelligence in Medical Imaging (CLAIM): A Guide for Authors and Reviewers. *Radiol Artif Intell*. 2020;2(2):e200029.
130. Shaikhina T, Khovanova NA. Handling limited datasets with neural networks in medical applications: A small-data approach. *Artif Intell Med*. 2017;75:51-63.
131. Vabalas A, Gowen E, Poliakoff E, Casson AJ. Machine learning algorithm validation with a limited sample size. *PLoS One*. 2019;14(11):e0224365.
132. Cohen J. *Statistical power analysis for the behavioral sciences*. 2 ed: Hillsdale: L. Erlbaum Associates; 1988. 567 p.

133. Fusco R, Granata V, Grazzini G, Pradella S, Borgheresi A, Bruno A, et al. Radiomics in medical imaging: pitfalls and challenges in clinical management. *Jpn J Radiol.* 2022;40(9):919-29.
134. van Timmeren JE, Cester D, Tanadini-Lang S, Alkadhi H, Baessler B. Radiomics in medical imaging-"how-to" guide and critical reflection. *Insights Imaging.* 2020;11(1):91.
135. Elmahdy M, Sebro R. Radiomics analysis in medical imaging research. *J Med Radiat Sci.* 2023;70(1):3-7.